Post-seismic motion after 3 Chilean megathrust earthquakes: A clue for a linear asthenospheric viscosity

H. Boulze[1], L. Fleitout[1], E. Klein[1] and C. Vigny[1]

[1] *Laboratoire de géologie - CNRS UMR 8538, École normale supérieure - PSL University, Paris, France*

SUMMARY

Over the last decade, three major subduction earthquakes, Maule M_w 8.8 (2010), Illapel M_w 8.3 (2015) and Iquique M_w 8.1 (2014), occurred in Chile and generated significant post-seismic deformations. These large scale and long lasting deformations can be quantified with modern GNSS precise positioning and highlight visco-elastic processes in the asthenosphere. Here, we calculate the ratios of cumulative post-seismic displacements after 5 years over the co-seismic offsets. We find that at any distance from the trench, ratios are similar for the three earthquakes despite their different magnitudes which imply induced stresses that are more than one order of magnitude apart. This observation suggests that the post-seismic deformation is related to the same effective viscosity for the

three earthquakes, indicating Newtonian rheology, rather than power-law rheology in the asthenosphere.

Key words: Creep and deformation; Numerical modelling; Seismic cycle; South-America; Subduction zone processes; Time-series analysis

1 INTRODUCTION

Large earthquakes induce stress changes in the mantle over large distances and depths. On a time-scale of a few years, only the part of the mantle with the lowest viscosity, named asthenosphere, is able to creep significantly. Thus, post-seismic deformation is a ”natural experiment” that constrains the rheology of the asthenosphere. The asthenosphere is below the thermal boundary layer which constitutes the lithosphere. The lithosphere, colder thus more viscous, is about 80 km thick for old oceans and non cratonic continents (e.g. Fleitout and Yuen, 1984; Doin and Fleitout, 1996). The thickness of the asthenosphere is poorly constrained, but, according to models of post-seismic deformation, it is thought to range between 100 km and 300 km (Trubienko et al., 2014). One of the most important questions that remains is whether the asthenospheric viscosity is stress dependent or not. In general, the answer to this question depends on the predominant creep mechanism in the asthenosphere (e.g. Weertman and Weertman, 1975; Karato, 2008). For example, dislocation creep is known to involve stress-dependent effective viscosity (Weertman, 1970) while diffusion creep is associated with linear rheology, i.e. a creep rate that is simply proportional to the deviatoric stress (Gordon, 1965). It was also pointed out that with a power-law rheology the medium can artificially appear linearly viscous during a non steady-state process if the background stresses induced by ’steady’ mantle convection are large enough (Schmeling, 1987).

Monitoring and quantification of surface deformation after a large earthquake by precise satellite

positioning (GNSS) should provide the means to quantify the viscous laws at play in the asthenosphere. However, while many studies have used a linear viscosity (e.g. Hu et al., 2004; Pollitz, 2005; Trubienko et al., 2013; Klein et al., 2016; Hu et al., 2016; Li et al., 2017), many others concluded that a power-law viscosity provides a better fit to post-seismic deformation (e.g. Pollitz et al., 2001; Freed and Burgmann, 2004; Freed et al., 2006; Barbot, 2018; Agata et al., 2019; Muto et al., 2019; Peña et al., 2019; Weiss et al., 2019; Peña et al., 2020). A somewhat surprising observation has been made regarding far-field post-seismic deformation after the three recent megathrust earthquakes of magnitude close to 9 (Sumatra, M_w 9.2, 2004; Maule, M_w 8.8, 2010 and Tohoku, M_w 9.1, 2011) in Trubienko et al. (2014). The observed co-seismic and post-seismic displacements as a function of time at continuous far-field GNSS stations were found to be nearly homothetic, independently of the earthquake magnitude and geological context. This result argues for a similar effective viscosity in the asthenosphere, at least in the far-field and for earthquakes of magnitude around 9. We expand here the magnitude range of this observation using the three recent Chilean subduction earthquakes of Maule 2010 (M_w 8.8), Illapel 2015 (M_w 8.3) and Iquique 2014 (M_w 8.1). We also investigate whether the observation is valid not only in far-field but at any distance from the trench and discuss the implications for the rheology of the asthenosphere.

2 GPS DATA

2.1 Data set and processing

South American networks provide a good coverage of co-seismic offsets and post-seismic displacements at the scale of the continent, at all distances from the trench. Networks are dense enough to allow us to pick stations near profiles perpendicular to the trench at the latitude of all three earthquakes. We use 52 continuous GPS stations facing the three ruptures zones, in near-field (100-300 km from the trench), mid-field (300-500 km) and far-field (500-1400 km) (Fig. 1A and Fig. S1). Station time-series

are extracted from *SOAM_GNSS_solENS*, the South American daily solution produced by Klein et al. (2022) based on observations provided by the CSN network in Chile (Baez et al., 2018), the RAMSAC network in Argentina (Piñón et al., 2018) and the IGM network in Bolivia. Daily coordinates are processed with the GAMIT/GLOBK suite (Herring et al., 2010a,b) and the PYACS toolbox. Twenty year time-series (2000-2020) are expressed in ITRF2014 (Altamimi et al., 2016).

2.2 Data analysis

We correct time-series from outliers, antenna offsets and earthquakes. We estimate co-seismic offsets differently depending on the signal/noise ratio. For high ratios we simply differentiate between the day after (three days for Iquique, Section S2.2) and the day before the earthquake. For low ratios, we estimate multi-day trends to compute average positions both before and after the earthquake. We define the post-seismic deformation as the difference between after and before the earthquake (cf a description of the whole seismic cycle in Trubienko et al. (2013)). Thus, we estimate pre-seismic trends and subtract them from the total displacement after the earthquake to extract the post-seismic signal (Section S2.1). We estimate the cumulative post-seismic displacement over 5 years after each earthquake. For high signal/noise ratios, we use the position one day after the earthquake at the beginning and the one week-average position at the end. For low signal/noise ratios, we use smoother parametric models. The estimation of the cumulative post-seismic displacement is sensitive to the estimation of the pre-seismic trend, especially in the far-field where numbers are small.

2.3 Analysis of the ratios of post-seismic displacements over co-seismic offsets

Co-seismic offsets decrease with distance from the trench and, as expected, the larger the earthquake the larger the offsets (Fig. 1B and Fig. S4). The cumulative post-seismic displacements also decrease with distance from the trench after an initial increase in near-field. Again, the larger the earthquake the

larger the displacements (Fig. 1C). On the contrary, ratios of cumulative post-seismic displacements (*post*) over co-seismic offsets (*co*), hereafter referred to as *post/co ratios*, increase with distance from the trench (Fig. 2A). Remarkably *post/co ratios* of all three earthquakes evolve in the same way and are superposed, despite different magnitudes and geometries (Fig. 2A). The *post/co ratios* are similar even for the Illapel earthquake where the presence of a flat slab does not seem to disrupt the horizontal deformation. This remains true over different time periods: the first two years when afterslip dominates near-field deformation as well as the last three years when visco-elastic deformation becomes dominant (see Section S4 for discussion on afterslip duration and impact).

In near and mid-field (at distances shorter than 500 km), uncertainties are small because displacements are large and *post/co ratios* fall well on the same linear trend. In the far-field (beyond 500 km), a decreasing trend seems to appear. However, the trend is here unclear because scattering is larger. Scattering increases with distance from the trench because displacements decrease with distance from the trench. For Illapel and Iquique, beyond 800 km both co-seismic offsets and cumulative post-seismic displacements go down to a few millimetres only, yielding less well determined ratios.

Post-seismic time series normalised by the co-seismic offsets also show the remarkable superposition independent of the earthquake size. In near-field, station MAUL (affected by Maule Eq.) and MNMI (affected by Iquique Eq.) superimpose extremely well (Fig. 2B). The same is true in far-field for station VBCA (affected by Maule Eq.) and EPSF (affected by Illapel Eq.) (Fig. 2C).

3 CONSEQUENCE FOR THE ASTHENOSPHERIC VISCOSITY

The *post/co ratios* are similar for the three recent Chilean mega-earthquakes, despite their different moments, different slip patterns and perhaps different asthenospheres. In principle, post-seismic displacements, co-seismic offsets and *post/co ratios* depend mainly on three parameters: The magnitude and slip distribution of the earthquakes that generated them, and the viscosity law of the asthenosphere

that carries the deformation. Our purpose here is not to present models that would closely fit the curves of *post/co ratios* (Fig. 2A). We simply want to explore the impact of the asthenospheric rheology on earthquakes of different magnitudes using simple models: In particular, we compare predictions based on power-law versus linear viscosities. In the finite-element numerical models used in this section, we deliberately suppress all the various supplementary ingredients (Burgers viscosity, low viscosity channel or low-viscosity wedge, post-seismic slip on the interface) already explored in Klein et al. (2016) concerning the Maule earthquake. In addition, following most previous studies, we assume that the stress in the asthenosphere is only generated by the earthquake itself. At this point, the only thing that matters is to predict *post/co ratios* independent upon the magnitude and slip pattern of the earthquake. Modeling details (slab geometry, boundary conditions, etc.) are given in Section S5.

We begin by recalling some general analytic scaling laws that involve time and rheology, which are exact only if one compares homothetic earthquakes, i.e. earthquakes with different magnitudes but with the same slip distribution. So, we first perform numerical tests to compare *post/co ratios* produced by homothetic earthquakes, using either Newtonian or power-law viscosity. Then, to approximate the real case, we compare *post/co ratios* produced by different co-seismic slip distributions (both along strike and along depth), combined with different magnitudes, again in the context of either Newtonian or power-law viscosity.

3.1 Asthenospheric viscosity and earthquake magnitude: analytical scaling relations from homothetic earthquakes

We consider here two earthquakes E1 and E2 with the same pattern of co-seismic slip, but different magnitudes (homothetic slips): At any point on the subduction interface, the ratio of the co-seismic slips is a constant factor λ. Because linear elasticity is involved, the ratio of the two co-seismic offsets at any point on the Earth's surface is then also λ. For a linear visco-elasticity in the asthenosphere

(Maxwell or Burgers), possibly variable spatially, but identical for the two earthquakes, the ratio of the post-seismic deformations is also λ everywhere and for all times. So: $co_{E2} = \lambda \cdot co_{E1}$ and $post_{E2}(t) = \lambda \cdot post_{E1}(t)$. The *post/co ratios* of the two earthquakes at a same point of the Earth surface and at a same time t are then equal at all times:

$$(post/co)_{E1}(t) = (post/co)_{E2}(t) \tag{1}$$

If the viscosities for the E1 earthquake are everywhere k times larger than the viscosities for the E2 earthquake, then this relationship becomes:

$$(post/co)_{E1}(kt) = (post/co)_{E2}(t) \tag{2}$$

In simple words, at any given point, the same strain will be reached after a time k-times longer if the viscosities are everywhere k-times larger.

For power-law viscosity we use the following creep law (e.g. Stocker and Ashby, 1973; Schubert et al., 1978; Schmeling, 1987):

$$\bar{\bar{\dot{\epsilon}}} = C(J_2(\bar{\bar{\tau}}))^{(n-1)/2}\bar{\bar{\tau}} \tag{3}$$

where $\bar{\bar{\dot{\epsilon}}}$ and $\bar{\bar{\tau}}$ are respectively the strain-rate and deviatoric-stress tensors and J_2 is the second invariant of the stress tensor 1/2 tr($\bar{\bar{\tau}}^2$). The stress exponent n varies between 2 and 6 but will be taken equal to 3 for further applications. The scalar C depends, in the mantle, upon temperature, pressure, water content, grain size, etc. It is then possibly variable spatially but assumed here to be the same for the two earthquakes which differ only by their magnitude. Then, the two *post/co ratios* are equal if the post-seismic motion of the smallest earthquake is computed at a time $\lambda^2 t$ (Section S6.1):

$$(post/co)_{E1}(\lambda^2 t) = (post/co)_{E2}(t) \tag{4}$$

In simple words, if the moment of E1 is λ-times smaller than the moment of E2, the same *post/co ratios* will be reached after a time λ^2-times larger.

Implications of Eqs. 1 to 4 for *post/co ratios* after 5 years are investigated through a synthetic nu-

merical example. Two fictive seismic sources with identical slip distributions but different magnitudes are used: i) a M_w 8.1 earthquake (Fig. 3A), ii) a homothetic (multiplied by 11.4) M_w 8.8 earthquake (Fig. 3B).

The curves of *post/co ratios* in the Newtonian rheology case are identical (Newtonian-E1 vs. Newtonian-E2) (Fig. 3D). On the contrary, the curves of *post/co ratios* in the non-Newtonian case differ largely (power-law-E1 vs. power-law-E2), by a factor of 10 (Fig. 3D). A direct illustration of Eq. 4 based on modelled time-series in case of power-law rheology is provided in Supporting Information (Fig. S8).

Numerical tests concur with the above analytical relationships. Both show that when the effective viscosity is the same, *post/co ratios* as a function of time and distance from the trench are equal, whatever the magnitude of earthquakes (assuming an identical slip pattern). The *post/co ratios* become strongly different when the effective viscosity differs either through power-law rheology or through linear but regionally variable viscosities in the asthenosphere (see Eq. 2, Eq. 4 and light red dot-dashed line in Fig. 3).

3.2 Asthenospheric viscosity, earthquake magnitude and slip distribution: numerical tests for non-homothetic earthquakes

We now consider the case of two earthquakes with non homothetic co-seismic slip distributions: the fictive M_w 8.1 earthquake (referred to as E1, Fig. 3A) and the real Maule earthquake M_w 8.8 from Klein et al. (2016) (referred to as E3, Fig. 3C). The Maule earthquake slip distribution presents patches extending from 32°S to 39°S and several deep slip patches (below 45 km depth). The fictive slip distribution of E1 corresponds to the main patch of Maule only, but with reduced N-S extent and without deep slip patches. So the magnitude is reduced but also the slip distribution is different.

The curves of the *post/co ratios* in the Newtonian rheology case are again almost identical (Newtonian-

E1 vs. Newtonian-E3, Fig. 3D). And likewise, the curves of the *post/co ratios* in the non-Newtonian case differ largely (non-Newtonian-E1 vs. non-Newtonian-E3, Fig. 3D), by a factor close to 10. So, the scaling laws described by Eqs. 1,2 and 4 can still be used, in first approximation, to compare the *post/co ratios* of earthquakes with co-seismic slip distributions that differ in both north-south lateral extent and average depth.

To better understand why the *post/co ratios* vary little with the co-seismic slip distribution, we plot, along the same profile the ratios of i) co-seismic offsets $(co(E3)/co(E1))$; ii) cumulative post-seismic displacement $(post(E3)/post(E1))$ and iii) von Mises stresses ($(\sqrt{(}3J_2)$ where J_2 is the second invariant of the stress tensor) at 200 km depth in the asthenosphere and at the date of the earthquake $\sigma(E3)/\sigma(E1)$ (Fig. 3E). These ratios would all be equal to the ratio of seismic moment (11.4 in this case) if the earthquakes were homothetic. In the far-field, they are close to the seismic moment ratio of 11.4, and slightly differ only because the average depth of the co-seismic slip for the two earthquakes differs (Fig. 3E). In the near-field, all three ratios decrease as we get closer from the trench since only a little fraction of the widespread source of Maule earthquake is acting. Therefore, relations between *post/co ratios*, exact in the homothetic case, remain approximately valid for realistically different earthquakes.

4 DISCUSSION AND CONCLUSION

This study highlights the striking similarities of the ratios of post-seismic displacements over co-seismic offsets after the three Chilean earthquakes. We propose a simple interpretation of these observations based on fairly basic models involving purely Newtonian or power-law rheologies.

The time-dependent stresses associated with the seismic cycle are in reality superimposed on the steady (i.e. steady over a time-scale of few 100 yrs) background stresses involved in plate-tectonics and global mantle convection. In case of power-law creep, the visco-elastic response to an earthquake

becomes coupled to these background stresses. If the deviatoric stresses associated with the earthquake cycle are smaller than the background stress, then the effective viscosity governing the post-seismic deformation becomes linear although anisotropic, as discussed in detail in Schmeling (1987) concerning Glacial Isostatic Adjustment (GIA). Assuming a background stress of 4×10^4 Pa corresponding to a 5 cm/yr velocity variation across a 200 km depth asthenosphere with a viscosity of 5×10^{18} Pa.s, the post-seismic deformation induced by Iquique and Illapel earthquakes would mostly happen under this linearized regime (Fig. S9). However, the stresses in the near and mid-field just facing the rupture zone of Maule would strongly exceed the background stress during the first years after the earthquake and the strong variability of the *post/co ratios* that we infer for the power-law case would persist. In the unlikely presence of background stresses larger than 10^5 Pa, the post-seismic deformations induced by the three earthquakes would occur under the linearized regime.

It seems difficult to argue for a smaller intrinsic viscosity in the area affected by Illapel and Iquique earthquakes, which would cancel the potential effect of a power-law viscosity. For example, the constant C in Eq. 3 would be multiplied by 100 in the area affected by Iquique and Illapel earthquakes because of conditions hotter or wetter than in the area affected by Maule earthquake. Actually, the seismic velocities in the asthenosphere (e.g. Feng et al., 2007; Celli et al., 2020), thought to be good indicators of temperature or water content, are slightly lower in the area affected by Maule earthquake, suggesting a somewhat lower intrinsic viscosity. Both power-law creep and the intrinsic effect would then lower the effective viscosity in the area affected by the huge Maule earthquake, making the misfit to data even worse. Such a large viscosity difference in front of the rupture zone of the three earthquakes is not supported by our observations.

Many studies favour power-law rheology to explain post-seismic deformation (e.g. Pollitz et al., 2001; Freed and Burgmann, 2004; Freed et al., 2006; Barbot, 2018; Agata et al., 2019; Muto et al., 2019; Peña et al., 2019; Weiss et al., 2019; Peña et al., 2020). The two main reasons invoked are ei-

ther an observation (significant long-term uplift of the volcanic arc after the Aceh, Tohoku or Maule earthquakes) or a model requirement (an apparent increase in effective viscosity with time). Indeed, models with uniform linear viscosity in the asthenosphere, a flat lithosphere-asthenosphere boundary and Maxwell rheology do not predict uplift in the volcanic arc and have difficulties to fit long time-series with a single viscosity. Power-law creep does induce short-term uplift in this region, but during a few months only. Any model involving a linear low viscosity wedge (Trubienko et al., 2014) or channel (Klein et al., 2016) also predicts long-term ($>$ 10 years) uplift on the volcanic arc, as observed. The visco-elasticity of the heterogeneous asthenosphere is unlikely to correspond to a Maxwell material, as demonstrated by the homogenization theory (Ivins and Sammis, 1996). The temporal increase in apparent viscosity can be explained by Burgers rheology. Post-seismic slip on the interface also contributes to a rapid initial deformation. Rapid deformation in the first months after the earthquake and uplift of the volcanic arc are predicted by a power-law type rheology but also by other rheological features of the asthenosphere. The comparison of deformations induced by stresses of very different magnitude (Maule vs Illapel and Iquique) provides a specific, so far unexplored argument in the debate between linear and power-law viscosity.

The surprising similarity of the *post/co ratios* as a function of time and distance from the trench for the three recent Chilean megathrust earthquakes suggests a rather uniform effective viscosity from North to South in the asthenosphere below the South American plate, south of 15° S. We find that power-law creep plays no significant role in post-seismic deformation, which can be actually modelled using linear rheology. It is somewhat more difficult to know whether these observations on the *post/co ratios* mean that the asthenospheric rheology governing long-term mantle deformation is also linear, as the answer to this question requires an estimate of the magnitude of the background stress. However, unless we have grossly underestimated the background stress, the similarity of the deformations in

the early stages after the Maule, Illapel and Iquique earthquakes indicates a linear rheology of the asthenosphere also for the long-term processes.

ACKNOWLEDGMENTS

We would like to thank CSN (Centro Sismologico Nacional), IPOC (Integrated Plate Boundary Observatory Chile), FENIX and CANTO (Central Andean Tectonic Observatory), RAMSAC (Red Argentina de Monitoreo Satelital Continuo), Bolivian IGM (Instituto Geográfico Militar), IGS (International GNSS service) for providing data from their respective geodetic networks. Maps are made with Generic Mapping Tools GMT (Wessel et al., 2019). The finite-element computations have been done using the Zset-Zébulon code (`http://www.zset-software.com/`). We thank J.D. Garaud for his help in particular for the 3D finite-element meshes. Finally, we thank our two reviewers and our editor Prof. Jörg Renner for their very constructive reviews. This work was supported by ANR grant number ANR-19-CE31-0003.

DATA AVAILABILITY

Time-series are publicly available (Klein et al., 2022).

SUPPORTING INFORMATION

Supporting_Information.pdf

References

Agata, R., Barbot, S., Fujita, K., Hyodo, M., Iinuma, T., Nakata, R., Ichimura, T., and Hori, T. (2019). Rapid mantle flow with power-law creep explains deformation after the 2011 tohoku mega-quake. *Nature Communications*, 10(1):1–11.

Altamimi, Z., Rebischung, P., Métivier, L., and Collilieux, X. (2016). Itrf2014: A new release of the international terrestrial reference frame modeling nonlinear station motions. *Journal of Geophysical Research: Solid Earth*, 121(8):6109–6131.

Baez, J. C., Leyton, F., Troncoso, C., del Campo, F., Bevis, M., Vigny, C., Moreno, M., Simons, M., Kendrick, E., Parra, H., et al. (2018). The chilean gnss network: Current status and progress toward early warning applications. *Seismological Research Letters*, 89(4):1546–1554.

Barbot, S. (2018). Asthenosphere flow modulated by megathrust earthquake cycles. *Geophysical Research Letters*, 45(12):6018–6031.

Celli, N., Lebedev, S., Schaeffer, A., Ravenna, M., and Gaina, C. (2020). The upper mantle beneath the south atlantic ocean, south america and africa from waveform tomography with massive data sets. *Geophysical Journal International*, 221:178–204.

Doin, M. and Fleitout, L. (1996). Thermal evolution of the oceanic lithosphere: an alternative view. *Earth and Planetary Science Letters*, 142(1-2):121–136.

Feng, M., van der Lee, S., and Assumpção, M. (2007). Upper mantle structure of south america from joint inversion of waveforms and fundamental mode group velocities of rayleigh waves. *Journal of Geophysical Research: Solid Earth*, 112(B4).

Fleitout, L. and Yuen, D. A. (1984). Secondary convection and the growth of the oceanic lithosphere. *Physics of the earth and planetary interiors*, 36(3-4):181–212.

Freed, A. and Burgmann, R. (2004). Evidence of power-law flow in the mojave desert mantle. *Nature*, 430:548–51.

Freed, A. M., Bürgmann, R., Calais, E., and Freymueller, J. (2006). Stress-dependent power-law flow in the upper mantle following the 2002 denali, alaska, earthquake. *Earth and Planetary Science Letters*, 252(3):481–489.

Gordon, R. B. (1965). Diffusion creep in the earth's mantle. *Journal of Geophysical Research*

(1896-1977), 70(10):2413–2418.

Hayes, G. P., Moore, G. L., Portner, D. E., Hearne, M., Flamme, H., Furtney, M., and Smoczyk, G. M. (2018). Slab2, a comprehensive subduction zone geometry model. *Science*, 362(6410):58–61.

Herring, T., King, R., and McClusky, S. C. (2010a). Gamit : Gps analysis at mit, release 10.4.

Herring, T., King, R., and McClusky, S. C. (2010b). Globk : Global kalman filter vlbi and GPS analysis program release 10.4.

Hu, Y., Bürgmann, R., Banerjee, P., Feng, L., Hill, E. M., Ito, T., Tabei, T., and Wang, K. (2016). Asthenosphere rheology inferred from observations of the 2012 Indian Ocean earthquake. *Nature*, 538(7625):368–372. Number: 7625 Publisher: Nature Publishing Group.

Hu, Y., Wang, K., He, J., Klotz, J., and Khazaradze, G. (2004). Three-dimensional viscoelastic finite element model for postseismic deformation of the great 1960 chile earthquake. *Journal of Geophysical Research: Solid Earth*, 109(B12).

Ivins, E. R. and Sammis, C. G. (1996). Transient creep of a composite lower crust: 1. constitutive theory. *Journal of Geophysical Research: Solid Earth*, 101(B12):27981–28004.

Karato, S.-i. (2008). *Deformation of earth materials*, volume 463. Cambridge Press Cambridge.

Klein, E., Fleitout, L., Vigny, C., and Garaud, J. (2016). Afterslip and viscoelastic relaxation model inferred from the large-scale post-seismic deformation following the 2010 Mw 8.8 Maule earthquake (Chile). *Geophysical Journal International*, 205(3):1455–1472.

Klein, E., Vigny, C., Nocquet, J.-M., and Boulze, H. (2022). A 20 year-long GNSS solution across South-America with focus in Chile. *Bulletin de la Société Géologique de France*, 193(1). 5.

Li, S., Moreno, M., Bedford, J., Rosenau, M., Heidbach, O., Melnick, D., and Oncken, O. (2017). Postseismic uplift of the andes following the 2010 maule earthquake: Implications for mantle rheology. *Geophysical Research Letters*, 44(4):1768–1776.

Muto, J., Moore, J. D. P., Barbot, S., Iinuma, T., Ohta, Y., and Iwamori, H. (2019). Coupled afterslip

and transient mantle flow after the 2011 tohoku earthquake. *Science Advances*, 5(9):eaaw1164.

Peña, C., Heidbach, O., Moreno, M., Bedford, J., Ziegler, M., Tassara, A., and Oncken, O. (2019). Role of Lower Crust in the Postseismic Deformation of the 2010 Maule Earthquake: Insights from a Model with Power-Law Rheology. *Pure and Applied Geophysics*, 176(9):3913–3928.

Peña, C., Heidbach, O., Moreno, M., Bedford, J., Ziegler, M., Tassara, A., and Oncken, O. (2020). Impact of power-law rheology on the viscoelastic relaxation pattern and afterslip distribution following the 2010 mw 8.8 maule earthquake. *Earth and Planetary Science Letters*, 542:116292.

Piñón, D. A., Gómez, D. D., Smalley Jr, R., Cimbaro, S. R., Lauría, E. A., and Bevis, M. G. (2018). The history, state, and future of the Argentine continuous satellite monitoring network and its contributions to geodesy in Latin America. *Seismological Research Letters*, 89(2A):475–482.

Pollitz, F. F. (2005). Transient rheology of the upper mantle beneath central alaska inferred from the crustal velocity field following the 2002 denali earthquake. *Journal of Geophysical Research: Solid Earth*, 110(B8).

Pollitz, F. F., Wicks, C., and Thatcher, W. (2001). Mantle flow beneath a continental strike-slip fault: Postseismic deformation after the 1999 hector mine earthquake. *Science*, 293(5536):1814–1818.

Schmeling, H. (1987). On the interaction between small- and large-scale convection and postglacial rebound flow in a power-law mantle. *Earth and Planetary Science Letters*, 84(2-3):254–262.

Schubert, G., Yuen, D. A., Froidevaux, C., Fleitout, L., and Souriau, M. (1978). Mantle circulation with partial shallow return flow: Effects on stresses in oceanic plates and topography of the sea floor. *Journal of Geophysical Research: Solid Earth*, 83(B2):745–758.

Stocker, R. L. and Ashby, M. F. (1973). On the rheology of the upper mantle. *Reviews of Geophysics*, 11:391–426.

Trubienko, O., Fleitout, L., Garaud, J.-D., and Vigny, C. (2013). Interpretation of interseismic deformations and the seismic cycle associated with large subduction earthquakes. *Tectonophysics*,

589:126–141.

Trubienko, O., Garaud, J.-D., and Fleitout, L. (2014). Models of postseismic deformation after megaearthquakes: the role of various rheological and geometrical parameters of the subduction zone. *Solid Earth Discussions*, 6:427–466.

USGS (Accessed: 2022-03-23). Earthquake Lists, Maps, and Statistics.

Weertman, J. (1970). The creep strength of the earth's mantle. *Reviews of Geophysics*, 8(1):145–168.

Weertman, J. and Weertman, J. R. (1975). High temperature creep of rock and mantle viscosity. *Annual Review of Earth and Planetary Sciences*, 3(1):293–315.

Weiss, J. R., Qiu, Q., Barbot, S., Wright, T. J., Foster, J. H., Saunders, A., Brooks, B. A., Bevis, M., Kendrick, E., Ericksen, T. L., Avery, J., Smalley, R., Cimbaro, S. R., Lenzano, L. E., Barón, J., Báez, J. C., and Echalar, A. (2019). Illuminating subduction zone rheological properties in the wake of a giant earthquake. *Science Advances*, 5(12):eaax6720.

Wessel, P., Luis, J. F., Uieda, L., Scharroo, R., Wobbe, F., Smith, W. H. F., and Tian, D. (2019). The Generic Mapping Tools Version 6. *Geochemistry, Geophysics, Geosystems*, 20(11):5556–5564. _eprint: https://agupubs.onlinelibrary.wiley.com/doi/pdf/10.1029/2019GC008515.

This paper has been produced using the Blackwell Scientific Publications GJI LaTeX2e class file.

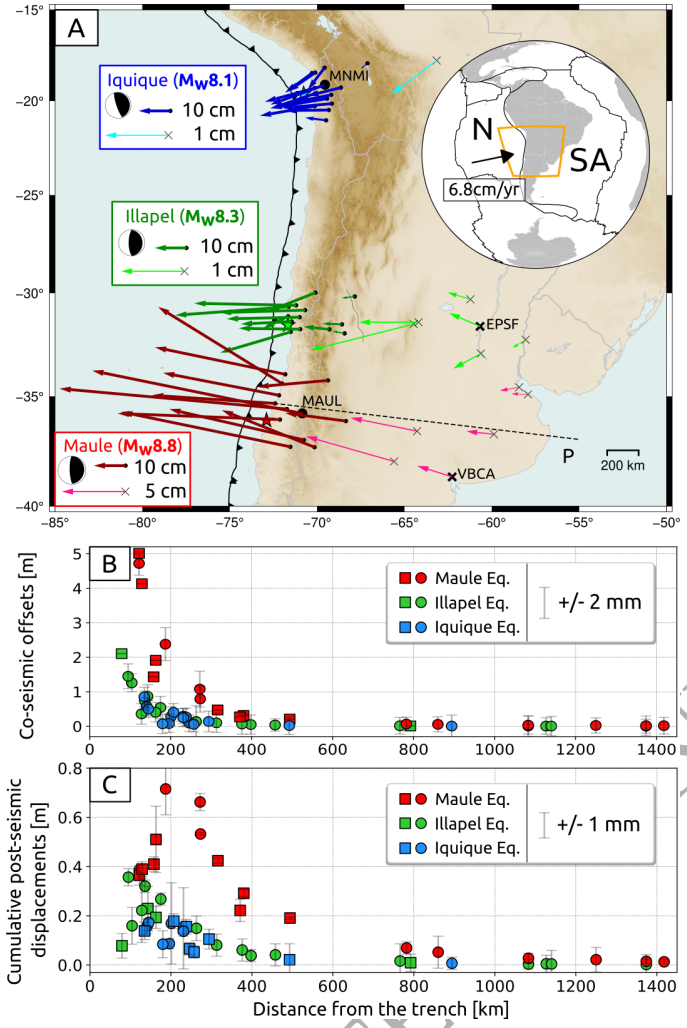

Figure 1. A-Cumulative post-seismic displacements (cm) after 5 yrs for Maule (red), Iquique (blue) and Illapel (green) earthquakes. Epicentres (stars) and focal mechanisms from USGS. The dashed line depicts profile P. The inset depicts the studied region (N=Nazca plate, SA: South-American plate). Evolution with distance from the trench of: B- co-seismic offsets (uncertainties are exaggerated 200 times) and C- cumulative post-seismic displacements over 5 yrs (uncertainties are exaggerated 50 times). B & C- Circles indicate stations where both co-seismic offsets and cumulative post-seismic displacements are measured while squares indicate stations where either co-seismic offsets or some of the post-seismic displacements are interpolated (missing data). All points have uncertainties, just hard to see if too small. Details about uncertainties are provided in Section S2.3. All values are summarised in Tables S1 and S2.

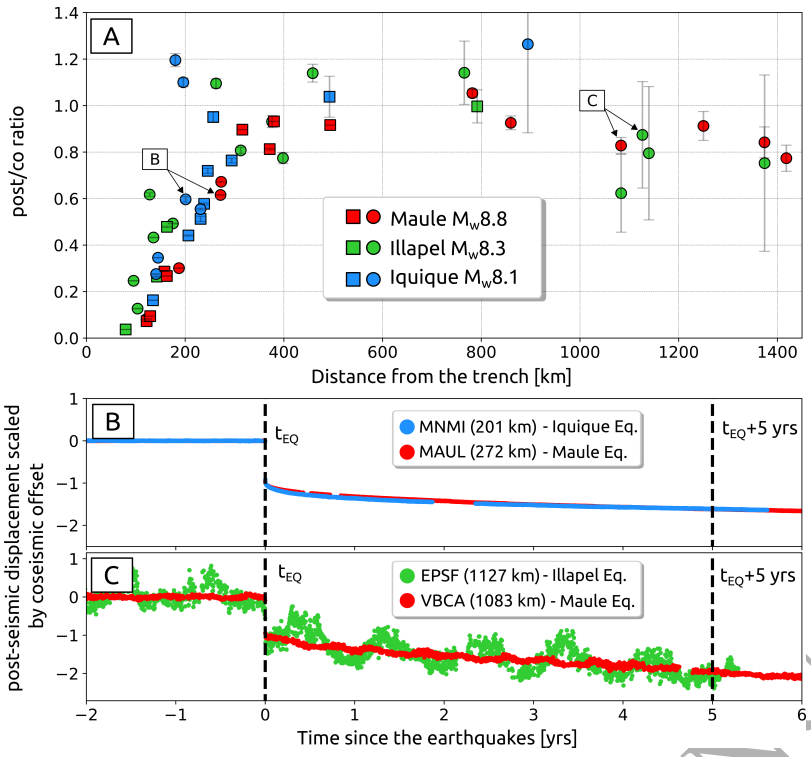

Figure 2. A- Evolution with the distance from the trench of the ratios of post-seismic displacements over co-seismic offsets for Maule (red), Illapel (green) and Iquique (blue) earthquakes. Circles and squares have the same meaning as in Fig. 1. All points have uncertainties, just hard to see if too small. East displacements scaled by co-seismic offset for two stations B- in near-field: MAUL (272 km, Maule Eq., in red) and MNMI (201 km, Iquique Eq., in blue) and C- in far-field: VBCA (1083 km, Maule Eq., in red) and EPSF (1127 km, Illapel Eq., in green). B & C- Pre-seismic trend subtracted, station distance from the trench indicated in legend.

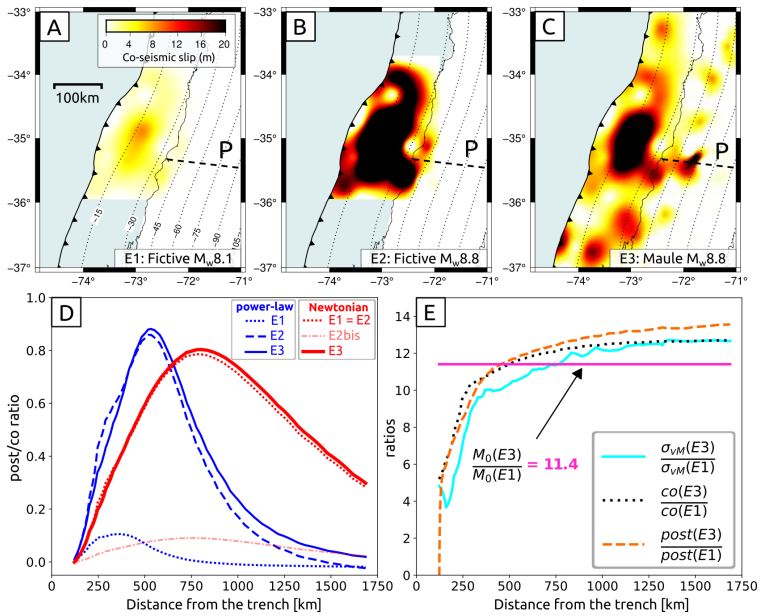

Figure 3. Co-seismic slip distributions of A-E1: Fictive M_w 8.1, B-E2: Fictive M_w 8.8 and C-E3: Maule M_w 8.8 (Klein et al., 2016) earthquakes. The colorscale is the same for the 3 slip distributions and is voluntarily saturated for B (max slip = 94m) and C (max slip = 45m). The dashed line at 35°S depicts the profile P along which curves of D and E are calculated (cf Fig. 1). The dotted lines depict the slab depth contours in km (Hayes et al., 2018). D- Evolution with distance from the trench of the *post/co ratios* over 5yrs, for E1 (dotted line), E2 (dashed line) and E3 (solid line) earthquakes predicted by a model with a Newtonian (4.75×10^{18} Pa.s) (red) vs a power-law (blue) asthenospheric viscosity. Note that the curves of E1 and E2 are identical in the Newtonian case. E2bis (light red dot-dashed line) depicts the *post/co ratios* obtained for the E2 slip distribution with a Newtonian viscosity 10 times higher (4.75×10^{19} Pa.s) E- Evolution with distance from the trench of the ratio between E3 and E1 earthquakes of the i) von Mises stresses (σ_{vM} - blue solid line) at 200 km depth at the time of the earthquakes; ii) surface co-seismic displacements (*co* - black dotted line); iii) 5-year cumulative post-seismic displacements (*post* - orange dashed line). The ratio of seismic moments (M_0) is indicated with a purple solid line.